Annals of Biomedical Engineering, Vol. 36, No. 11, November 2008 (© 2008) pp. 1870–1882
DOI: 10.1007/s10439-008-9556-2

Effects of Differences in Nasal Anatomy on Airflow Distribution: A Comparison of Four Individuals at Rest

REBECCA A. SEGAL,[1] GRACE M. KEPLER,[2] and JULIA S. KIMBELL[3]

[1]Department of Mathematics and Applied Mathematics, Virginia Commonwealth University, 1001 West Main St., PO Box 842014, Richmond, VA 23284-2014, USA; [2]Center for Research in Scientific Computation, North Carolina State University, Raleigh, NC, USA; and [3]The Hamner Institutes for Health Sciences, Research Triangle Park, NC, USA

(*Received 18 December 2007; accepted 25 August 2008; published online 6 September 2008*)

Abstract—Differences in nasal anatomy among human subjects may cause significant differences in respiratory airflow patterns and subsequent dosimetry of inhaled gases and particles in the respiratory tract. This study used computational fluid dynamics (CFD) to study inter-individual differences in nasal airflow among four healthy individuals. Magnetic resonance imaging (MRI) scans were digitized and nasal-surface-area-to-volume ratios (SAVR) were calculated for 15 adults. Two males and two females, representative of the range of SAVR values, were selected for flow analysis. Nasal CFD models were constructed for each subject by a semi-automated process that provided input to a commercial mesh generator to generate structured hexahedral meshes (Gambit, Fluent, Inc., Lebanon, NH, USA). Steady-state inspiratory laminar airflow at 15 L/min was calculated using commercial CFD software (FIDAP, Fluent, Inc., Lebanon, NH, USA). Streamline patterns, velocities, and helicity values were compared. In all subjects, the majority of flow passed through the middle and ventral regions of the nasal passages; however, the amount and location of swirling flow differed among individuals. Cross-sectional flow allocation analysis also indicated inter-individual differences. Laboratory water–dye experiments confirmed streamlines and velocity magnitudes predicted by the computational model. These results suggest that significant inter-individual differences exist in bulk airflow patterns in the nose.

Keywords—Computational fluid dynamics, Nasal airflow simulation, Flow experiments, Flow visualization, Human, Inspiratory airflow.

INTRODUCTION

The nasal passages are the main portal of entry for inhaled materials under most activity conditions. The nose not only filters, warms, and humidifies inhaled air, but also has a significant capacity for metabolism and clearance of inhaled materials to cleanse the inhaled air before it reaches the more delicate pulmonary airways.

Differences in nasal anatomy among human individuals lead to differences in airflow patterns within the nose and subsequently may cause significant differences in regional uptake of inhaled material within the respiratory tract. The increased sensitivity of some individuals to chemical exposure and changes in air quality could be due in part to higher regional nasal dosimetry. Nasal uptake is affected by factors such as individual anatomy, composition of the mucous and tissue lining of the respiratory tract, breathing patterns, and genetic factors affecting the capacity for metabolism and clearance of inhaled matter. Understanding the dosimetry of inhaled material is of primary importance for quantifying these differences. Since gases and particles are carried into the nose via inhaled air, measurement and comparison of airflow patterns is a necessary first step in addressing this issue.

The nasal passages contain features such as the nasal vestibule, nasal valve, turbinates, olfactory region, and nasopharynx which define the airspace. Although these features may differ slightly in size, shape and starting location from person to person, the main structural characteristics of the nose are consistent between individuals.[17] Anatomical and flow variability has been shown *in vivo* using acoustic rhinometry and rhinomanometry measurements of cross-sectional area and nasal resistance[10,22,23] and in studies of cadavers.[17] Variations in nasal anatomy can be seen throughout the healthy adult population and are likely to be even more pronounced among individuals with nasal abnormalities. The extent to which these anatomical differences affect airflow patterns and subsequently the filtering abilities of the nose have not been quantified. To predict individual risk, one needs to

Address correspondence to Rebecca A. Segal, Department of Mathematics and Applied Mathematics, Virginia Commonwealth University, 1001 West Main St., PO Box 842014, Richmond, VA 23284-2014, USA. Electronic mail: rasegal@vcu.edu

understand whether differences in airflow can be determined by external physical measurements (such as body size or ventilation parameters), or even by information available from medical imaging data (such as cross-sectional area or nasal-surface-area-to-volume ratio, SAVR).

Many studies have examined airflow patterns in the nasal cavity. Techniques have included computational fluid dynamics (CFD)[5,6,14,16,18,19,21,25,26,27,28] and particle image velocimetry (PIV),[4,11,13,15,24] but these studies are limited because they focused on single individuals. No systematic study has been conducted to date to examine variations in airflow patterns among individuals.

The study described here uses consistent techniques, both experimental and computational, to create nasal models from four different human subjects and compare steady-state inspiratory airflow patterns among these individuals. Three-dimensional (3D) computational models are used to provide detailed predictions regarding flow patterns, velocity and pressure values, and allow quantitative comparisons of these flow features among the four subjects. These results represent a first step toward testing the extent to which variability in susceptibility to inhaled materials is due to inter-human variation in nasal airflow.

METHODS

Anatomical Basis for Nasal Model Construction

The nasal models presented here were constructed from coronal magnetic resonance imaging (MRI) scans collected by Guilmette and colleagues.[10] Briefly, 45 healthy adult subjects were scanned at 3 mm increments for the entire nasal passageway. The data were examined for quality and scans were rejected if the nose was found to be at an extreme point in the nasal cycle in order to minimize potential confounding effects of the nasal cycle on anatomical differences among individuals. Coronal sections of the nasal airway were digitized by hand tracing and the ratio of surface area to volume from the nares to the posterior end of the nasal septum was calculated for the 15 nasal passages which included a well-defined olfactory region. Three subjects, designated 12, 14, and 18, were selected for this study (Table 1) because their SAVR represented a range of values. Coordinate data points representing each cross-sectional outline were ordered to form a continuous path around the outline of the cross section and 3D reconstructions of the cross sections were made. A fourth subject, A, had been modeled in previous work[26] and was included for comparison in this study.

TABLE 1. Human subject data.

Subject number	Sex	Height (cm)	Weight (kg)	Surface area (mm^2)	Volume (mm^3)	Nasal SA/V (mm^{-1})
A	Male	173	73.0	18,363	17,126	1.07
12	Female	160.7	55.7	15,795	15,305	1.03
14	Male	186.1	74.0	20,714	21,957	0.94
18	Female	170.2	61.2	19,850	23,409	0.85

Surface areas (SA) and volumes (V) were calculated from the nostrils to the end of the septum.

Computational Mesh Construction

The migration of medical data such as MRI or CT scans (Fig. 1a) to a computational mesh of the nasal passages requires several steps. In the process used here, the nasal passages were identified on each medical image and the outline of the airspace for each airway image was digitized by hand tracing. This process captured x,y-coordinates in a continuous path along the airway perimeter of each coronal cross section (Fig. 1b). A separate computer file of coordinates was made for each cross-sectional data set and labeled according to its axial location.

Automatic hexahedral mesh generation using commercial mesh generators has not proven successful on the complex geometry of the nose, yet hexahedral elements for such meshes are desirable for simulation accuracy.[20] The use of unstructured tetrahedral meshes may introduce artificial diffusion due to element faces not aligning with the main flow field, so we invested the time to develop structured hexahedral elements.

To construct computational meshes from sequential cross-sectional data containing hexahedral elements, a new semi-automated process (MAesh) was developed in-house using Matlab (The MathWorks, Inc., Natick, MA, USA). MAesh was used to spline the boundary of each digitized cross section, and to select anchor points for the computational mesh, called keypoints, along each boundary (Fig. 1c). The keypoints from each series of nasal cross sections were used to decompose the complex nasal geometry into a large number of much simpler 3D volumes that could be meshed using an automatic hexahedral process.

In addition to the keypoint identification, MAesh was used to specify the mesh density and to create special regions on the nasal boundary such as nostrils, outlet, and walls to be used in specifying boundary conditions for flow simulations. Mesh density was set so that all airways were spanned by at least four mesh elements. MAesh was then used to generate a file of commands formatted for the commercial mesh generation software Gambit (Fluent, Inc., Lebanon, NH,

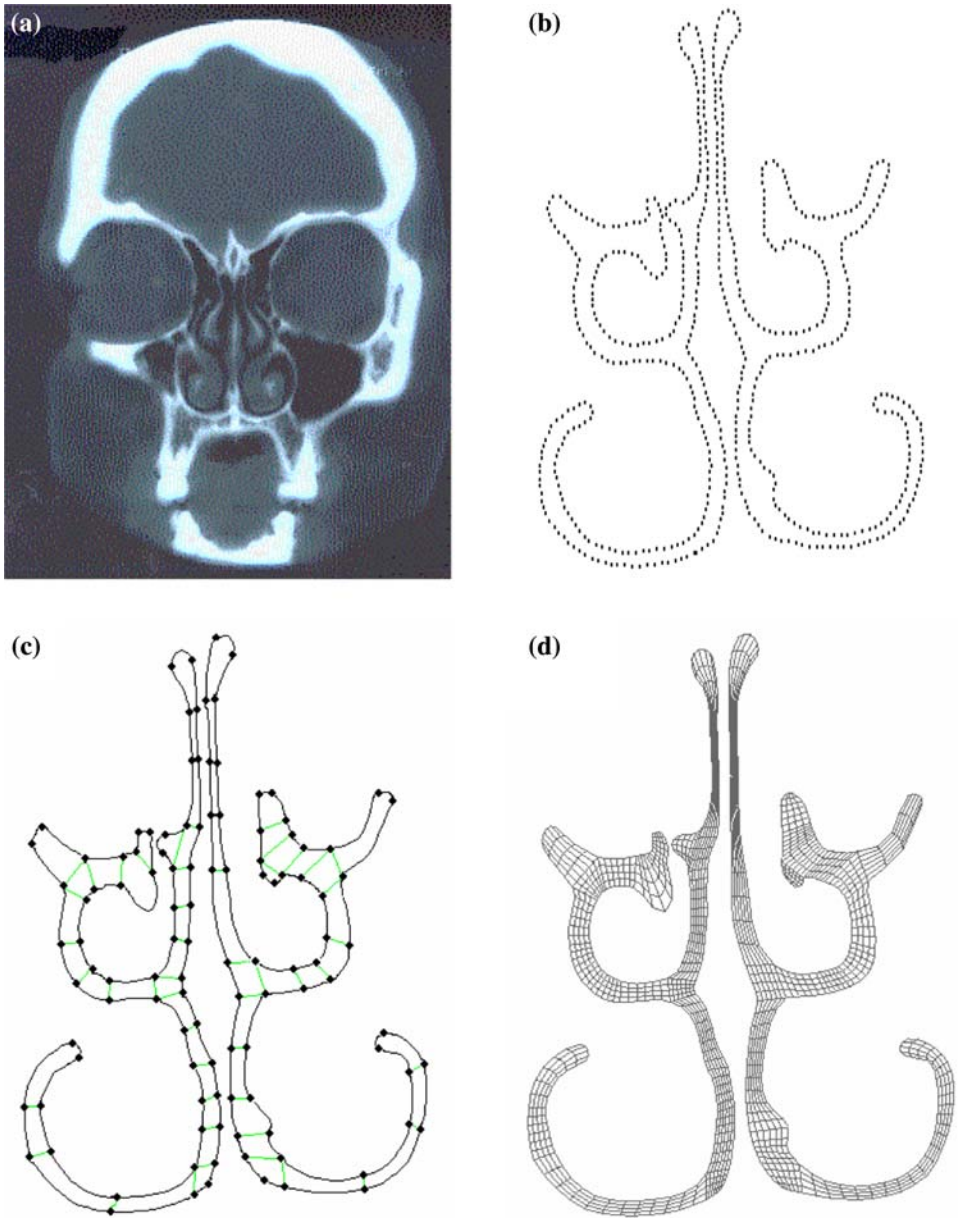

FIGURE 1. Transformation of medical data to a computational mesh. (a) Medical data illustrated by a CT scan image of the human head. The dark, curling regions in the center of the image are the airspaces of the nasal passages. (b) A digitized airway outline from one coronal cross section of an MRI scan. (c) Meshing keypoints (*black dots*) for the cross section shown in (b). (d) Final two-dimensional section mesh for the cross section shown in (b) with keypoints as shown in (c).

USA) which was used to generate two-dimensional cross-sectional meshes first (Fig. 1d) and then 3D computational meshes by connecting sequential cross-sectional meshes together. The number of hexahedral elements generated for each mesh is given in Table 2.

Addition of the Nasopharynx

Due to the coarse level of resolution in the axial direction of the coronal MRI scan sets, the nasopharynx of each individual was not clearly defined and was initially omitted. This omission meant that the posterior end of each CFD model consisted of a vertical section near the start of the nasopharynx region which was to be designated as the outlet of the model. However, for further studies using these models it will desirable to have a nasopharynx region. Therefore, a semi-artificial nasopharynx region was added to each model. The CFD model of Subject A had a nasopharynx and was used as a template to supplement the existing coarse resolution data for each subject so that the posterior end of each model was extended axially

and vertically to approximate a nasopharynx region (Fig. 2).

Simulations

It is common to assume a standard breathing rate corresponding to a specified activity level, so the airflow simulations for this study were conducted for steady-state inspiratory flow at rates of 7.5, 15, and 20 L/min for each individual, corresponding to resting breathing conditions.[1] Since we found similar flow patterns for all flow rates investigated, we focus this report on the 15 L/min simulations. Also, given the similarity of flow results across flow rates, it was desirable to isolate the geometry as the only variable and to fix the flow rate across subjects to allow for comparison of flow patterns.

TABLE 2. Geometry and flow parameters for simulations.

Subject	Hydraulic diameter of nostril (mm)	Re at 15 L/min	Mesh size (number of elements)
A	6.075	946.5	285,358
12	8.310	1321.8	340,776
14	7.942	1016.3	183,648
18	5.804	1605.6	171,360

The flow simulations were conducted using the finite element solver FIDAP (Fluent, Inc., Lebanon, NH, USA). As in previous work,[16,26] a uniform velocity field was defined on the nostril surfaces, a stress-free pressure condition was applied at the outlet, and zero velocity was specified at airway walls. The effect of the inlet velocity profile dissipates after the nasal vestibule,[14] making the choice of a uniform inlet profile reasonable for comparison purposes. For each model, the Reynolds number (Re) which is a constant resulting from nondimensionalizing the Navier–Stokes equations,[2] was computed. The Reynolds number is given by LU/v, where L is a characteristic length scale of the model, U is a characteristic velocity of the flow, and v is the kinematic viscosity of the fluid. In order to be consistent with previous work conducted with Subject A,[26] the length scale, L, in the Reynolds number was calculated based on the hydraulic diameter of the nostrils (4 × area/perimeter; Table 2). Each model was nondimensionalized based on this characteristic length and the nondimensional Navier–Stokes equations were solved to provide faster numerical convergence. The solution was achieved using a segregated solver algorithm with upwinding discretization scheme.[8] The results from the numerically converged simulations were redimensionalized prior to analysis.

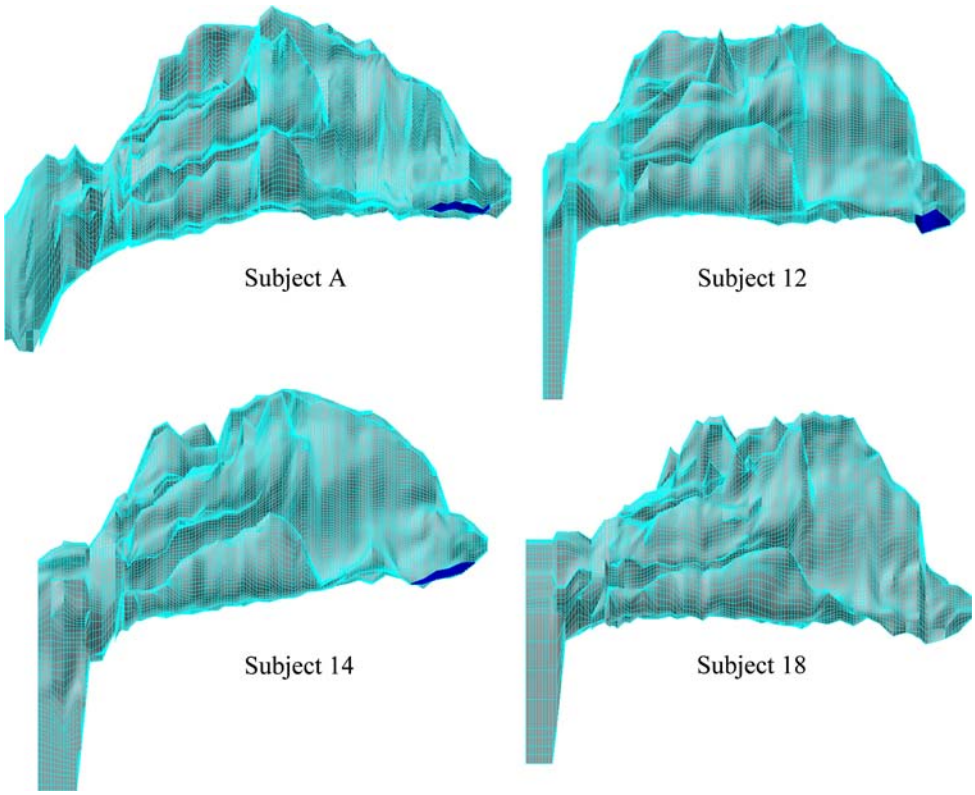

FIGURE 2. Computational meshes for Subjects A, 12, 14, and 18. Nostrils are shown in *blue* on the right side of the models and the nasopharynx is on the left.

Post-Processing

The flow visualization and analysis software package FieldView (Intelligent Light, Inc., Rutherford, NJ, USA) was used to visualize and post-process the flow simulations. Flow patterns were studied using streamlines (the paths that massless particles would follow if released into the flow), velocity vector plots and helicity calculations. Streamlines were generated from 30 randomly placed seed points on the nostril surface of each model and plots made in which streamlines were colored by flow magnitude using the same color scale for all four models. Examination of streamlines reveals some swirling flow.

To quantify swirling flow, helicity was examined. Following the work of Grigioni *et al.*,[9] we computed the mean normalized helicity Φ for each model, where

$$\Phi = \frac{1}{N_{\text{path}}} \sum_{k=1}^{N_{\text{path}}} \frac{1}{N_k} \sum_{j=1}^{N_k} \left| \Psi_{kj} \right|_j \tag{1}$$

and,

$$\Psi = \frac{\mathbf{V} \cdot (\nabla \times \mathbf{V})}{|\mathbf{V}||\nabla \times \mathbf{V}|}. \tag{2}$$

Here $\mathbf{V}$ is the velocity vector and the quantity $\mathbf{V} \cdot (\nabla \times \mathbf{V})$ is the helicity of the flow. The mean quantity Φ is the average of Ψ for 30 streamlines (N_{path}) for each model where N_k are the individual data points along a given streamline. The streamlines were partitioned into the different regions (vestibule, turbinate, and nasopharynx) and Φ was computed for each region. To confirm that the helicity calculation was not sensitive to location and number of seed points, a further calculation was performed using 100 randomly placed points. The results were comparable to the calculation with 30 seed points.

Regional divisions were used for further flow rate analysis (Fig. 3). The choice of cuts was made based on anatomical features. Cut A (Vestibule cut) separated the vestibule from more posterior regions. This cut is in the vicinity of the nasal valve, prior to the start of the turbinates. Cut B (Turbinate cut) was chosen so that inferior, middle, and superior turbinate regions were discernible. Cut C (Nasopharynx cut) was the plane of transition from the turbinate region to the nasopharynx region, near the termination of the nasal septum. Because of the coarseness of the data, Cut C had to be moved forward in Subjects 14 and 18. Each cross section was divided into a dorsal, middle, and ventral

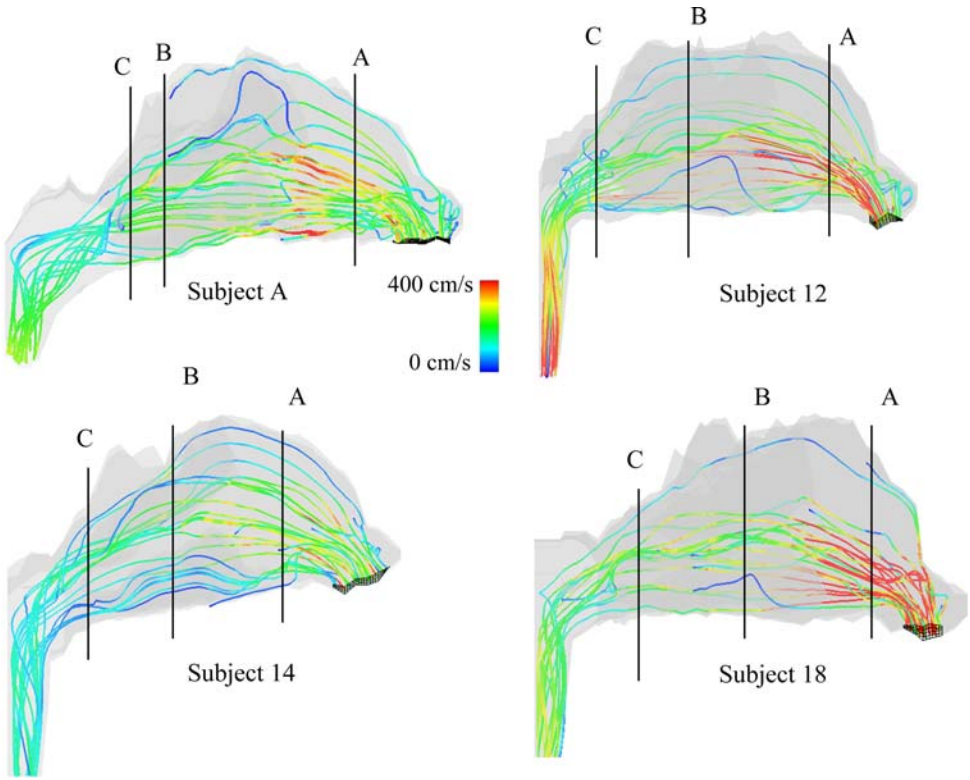

FIGURE 3. Flow streamlines for Subjects A, 12, 14, and 18, originating from the nostril traveling through the nose from right to left and exiting at the end of the nasopharynx. The streamlines are colored to describe the relative speed of flow with red for fast and blue for slow. Cut planes: A = Vestibule cut, B = Turbinate cut, and C = Nasopharynx cut.

region. The airflow through each of these regions was computed by integrating the axial component of velocity over the coronal cross section. These flow volumes were used to estimate the relative flow allocation within each region of the cross section as a percent of total volumetric flow for that cross section.

In addition, local Reynolds numbers for the dorsal, middle, and ventral sections of each Cut were calculated for Subject A for comparison among these regions. The calculation of the local Reynolds number was determined using the hydraulic diameter of the region for the characteristic length and the average velocity of the region for the characteristic velocity.[3]

Experimental Confirmation

Simulation accuracy for Subject A was previously described by Subramaniam and collaborators.[26] For Subjects 12, 14, and 18, laboratory experiments were conducted using water–dye streaklines to check computational flow simulation accuracy. Hollow plastic replicas of each computational mesh were created using stereolithography. The stereolithography method applied here used a laser sintering process to build the model one layer at a time in light sensitive polymer. The resulting transparent, hard, plastic models were exact replicas of the computational meshes to within the accuracy of the build layer thickness of 102 μm.[12]

A clear, acrylic tank was filled with water and the hollow models were submerged in the tank and held in place using a clamp (see Fig. 4). The tank was placed in a large tray so that the water level could overflow the tank thereby keeping a constant head of water. A hose clamp was used to regulate the flow rate as water was pulled from the nasopharynx section of the model at a constant rate of 1 L/min (dynamically similar to 15 L/min of air). The flow rate was monitored by a flow meter. The inflow water hose was placed in a large beaker at the side of the tank opposite the model to minimize the effect of disruptive currents on flow patterns inside the model.

To perform water–dye streakline experiments, a syringe filled with a solution of 1% aqueous basic fuchsin dye was positioned at the nostril openings of the model and held in place using a micromanipulator. This allowed the syringe tip to be moved around the surface of the nostrils so that dye could be released at any point. Dye was released using constant pressure applied by a syringe pump. In each model, clearly defined dorsal, middle, and ventral streaklines were recorded using digital video for measurement of flow velocities and flow patterns.

To provide accuracy in the comparison between the experimental streaklines and computational streamlines, it was important to match points of comparison sagittally as well as coronally and axially. Therefore, for each dorsal, middle, and ventral streakline, the position of the dye syringe at the nostril was recorded. Seed points in similar locations on the nostril surfaces of the simulations were identified and used to generate streamlines corresponding to each experimental streakline. Frame-by-frame video analysis was used to estimate the sagittal projection of flow velocity at two points along each streakline (corresponding to Cuts A and B; see Fig. 3). These measured velocities were compared with sagittal plane velocities calculated at Cuts A and B on each matched simulated streamline.

In a separate experiment, the pressure difference between the inlets and outlets of the nasal molds was measured using a digital pressure meter (VelociCalc Plus, Model 8386, TSI Inc., Shoreview, MN, USA). Pressure was measured for constant airflows pushed into the nostrils in the inspiratory direction at flow rates between 5 and 75 L/min. These flow rates were monitored using a mass flow meter (MFM, Model 4040, TSI Inc., Shoreview, MN, USA). Pressure was measured at a few centimeters from the inlet and outlet of the airways using a tube with an inner diameter of 3.175 mm positioned in a T-shaped fitting such that airflow did not enter the probe. During experiments the outlets of the replicas were open to room air.

RESULTS

General Flow Patterns

For each model simulation, a series of streamlines were generated (Fig. 3) from 30 randomly distributed seed points on the nostril surface of each model. The streamlines were colored by velocity magnitude with red representing the fastest flow (400 cm/s) and blue the slowest (0 cm/s).

A comparison of the streamlines indicated that in all subjects the majority of inspiratory flow was smooth in appearance and passed through the middle and ventral regions of the nasal passages. Inspiratory flow velocities were highest in the nasal vestibule and nasal valve regions in all models, discounting velocities near the semi-artificial outlets of Subjects 12, 14, and 18. Swirling flow was most evident in the nasal vestibule and nasopharynx of all subjects, but appeared to differ in intensity among the four individuals.

Velocity Vectors

A more detailed examination of the velocity field revealed that the maximum value for the bulk flow velocity for each model is located near the nasal valve region. This is expected since the nasal valve is the region of minimum cross-sectional area (Table 3).

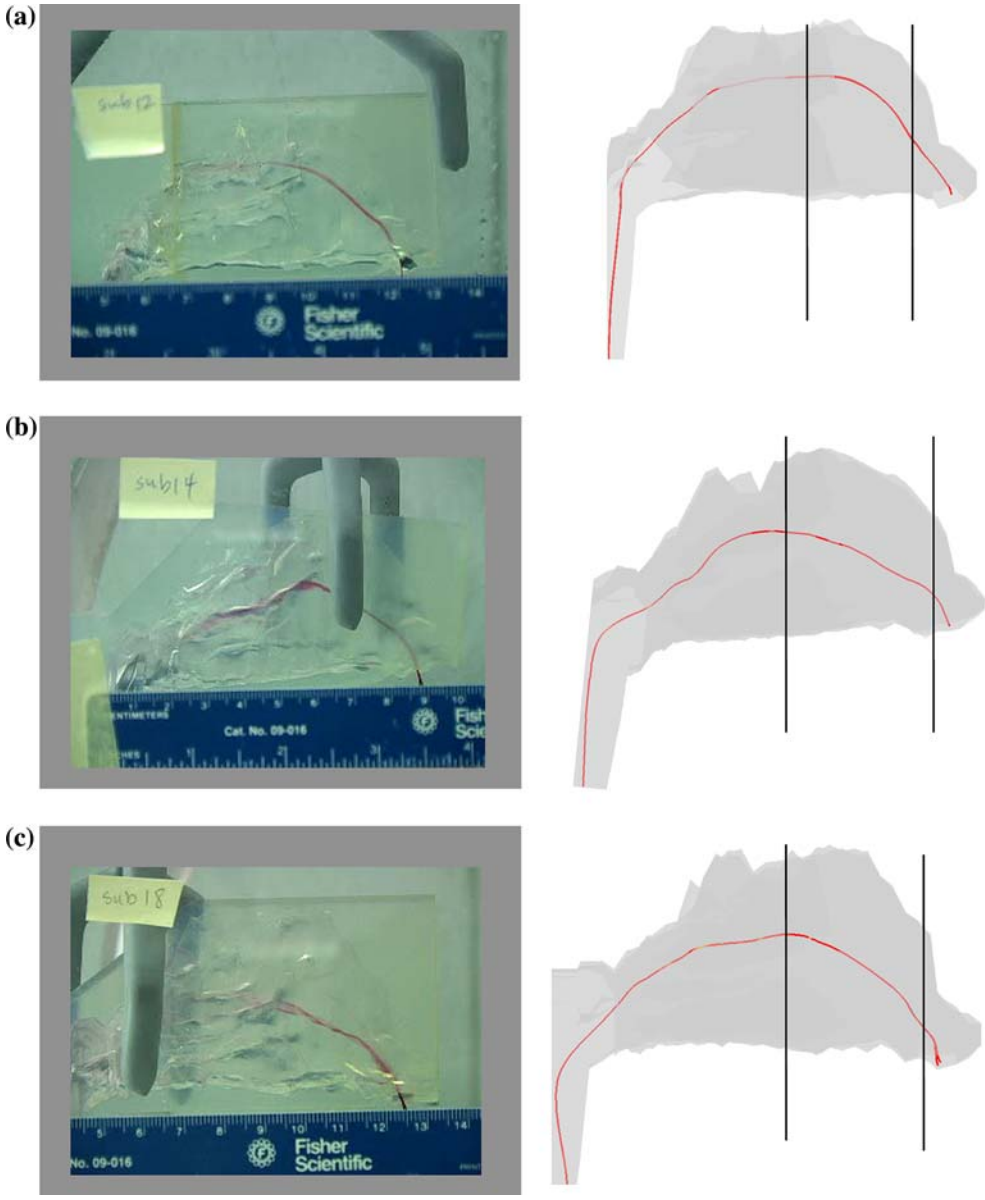

FIGURE 4. Comparison of experimental and computational middle streamline for Subject 12 (a), Subject 14 (b), and Subject 18 (c). The vertical lines indicate the location of velocity value sampling.

Using Fieldview, we computed the mean normalized helicity Φ to get a measure of the swirling motion present in the different regions of the nose (Fig. 5). This gives a quantitative measure of the qualitative results observed in the streamlines in Fig. 3. From Fig. 3, we can confirm that Subjects A and 18 do have increased circulation in the vestibule region. All subjects show increased swirling in the nasopharynx, with A and 12 having the largest amount of helicity. Subjects A and 14 have the smoothest flow through the turbinate region, although all subjects have the least amount of swirling in this region.

Regional Flow Allocation

Using dorsal, middle, and ventral divisions on vestibule, turbinate, and nasopharynx cross sections for each subject (Fig. 6), quantitative determinations of flow allocation confirmed that in all subjects, more flow passed through the middle and ventral regions than the dorsal region (Table 4). Region divisions were mainly determined by the location of the turbinates on each side of the nose but because of slight variations in turbinate position between left and right sides, the cut location varied slightly on either side of each nose. In the vestibule and the nasopharynx regions, flow

TABLE 3. Location of maximum *z*-component (direction of bulk flow) of velocity compared with minimum vertical cross-sectional area post-nostrils.

Subject	*z*-Coordinate maximum velocity (cm)	Maximum *z*-velocity (cm/s)	*z*-Coordinate minimum area (cm)
A	9.1	570.8	9.3
12	6.1	522.5	5.6
14	7.1	459.3	7.4
18	7.6	798.6	7.3

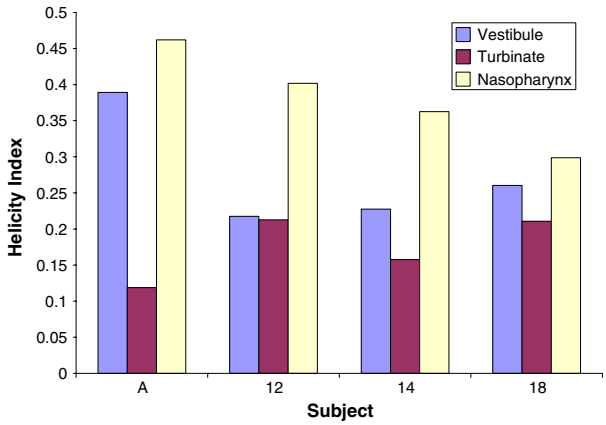

FIGURE 5. Comparison of helicity index values across the four subjects. The values are calculated for each nasal region with vestibule indicating the region from the nose tip to cut A, turbinate is the region between cut A and cut C, and nasopharynx is the region from cut C to end of the nasal passages.

allocation generally corresponded with cross-sectional area allocation (Fig. 7). The one exception is for Subject 12 in the vestibule. In this case, the cross-sectional area is the largest in the ventral region, but the flow allocation is maximal for the middle region. On the Turbinate cut plane however, there was not direct correspondence between the area and flow allocations. Only for Subject A were the trends related. For the other subjects, cross-sectional area measurements offered little insight into the relative changes in flow allocations.

In the turbinate region, Subject 12 was determined to have the most flow to the dorsal region compared to the other subjects. The flow to the middle region of Subject 12 was subsequently reduced compared to the others as a result of the higher dorsal flow. The other subjects are similar to each other in their allocations, with the smallest flow passing through the dorsal region. Flow in Subjects A, 14, and 18 was predicted to favor the middle region over the ventral region, but there was still an average of 40% of the flow traveling through the ventral region due to low flow in the dorsal region.

Local Reynolds numbers for the flow allocations areas in Subject A ranged from 46 in the dorsal turbinate area to 559 in the ventral vestibule (Fig. 6). The variation in local Reynolds number closes follows the variation in flow allocations. Because the Reynolds number is dominated by the velocity scale, which is determined from the average velocity of the flow through the region.

Experimental Confirmation

For each dorsal, middle, and ventral streakline, streamlines originating from seed points located at the streakline-specific nostril positions of the dye syringe matched the shape and location of the streaklines very well (Fig. 4). Projections of simulated velocity vectors onto the sagittal plane agreed with measured velocity projections to within 15% (Table 5).

Comparisons of pressure drop showed good agreement between the experiments and the computations (Fig. 8). Comparison of the data from Table 1 shows little correlation between the subjects' physical measurements and the relative values of the pressure drops across their nasal passages, although the two smallest nasal passages in volume did have the highest pressure drops.

DISCUSSION AND CONCLUSIONS

The goal of this work was to compare patterns of airflow in the nasal passages of four individuals. These comparisons provide preliminary information about potential differences in health risk across the population from inhaled material. Four nasal models were constructed based on MRI scans of human subjects and airflow patterns were computed and compared. Laminar airflow simulations conducted in all four nasal models at 15 L/min airflow rate, which were confirmed with an experimental flow study. Additionally, all subjects carried the bulk of the airflow through the middle and ventral regions of the nasal passages. This study indicated that, in these four individuals, variations in regional flow patterns and flow allocations were not completely predicted by external physical measures, SAVR or regional cross-sectional area calculations.

Model Construction

This study would not have been possible without access to the MRI data set of Guilmette and colleagues,[10] but these data presented some modeling challenges. First, the data set is more than a decade old and was, therefore, only available in hardcopy as sets of films. This meant that the data had to be hand digitized. Second, the data set was coarse. The images were taken at 3 mm increments. Third, for most of the

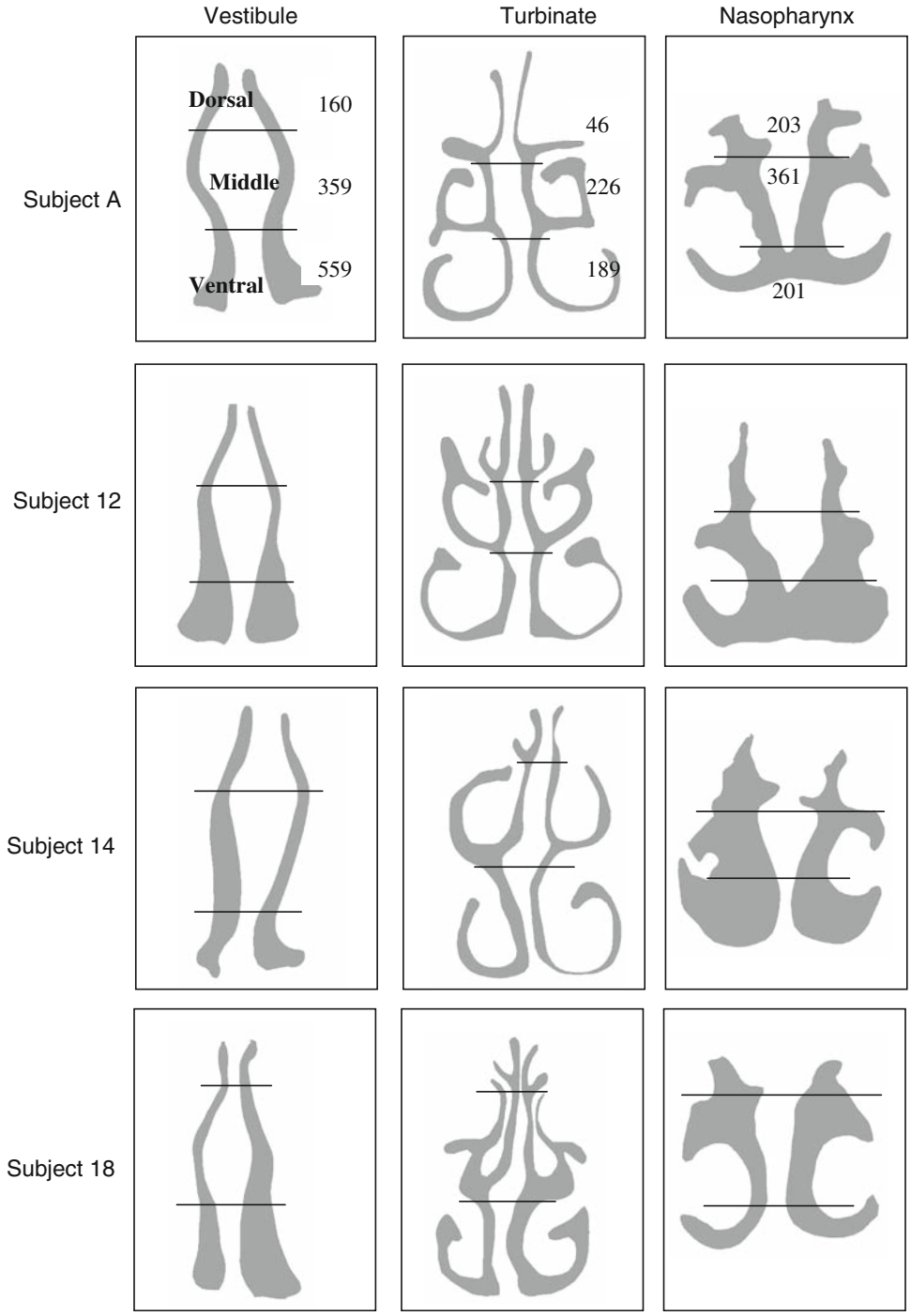

FIGURE 6. Diagram of nasal regions of interest for flow allocation calculations. Lines show approximate cut locations. Numbers on regions for Subject A indicate local Reynolds number values.

subjects, the imaging stopped short of the end of the nasopharynx region. The development and use of our automated meshing algorithm (MAesh) allowed us to cope with the first two difficulties. The program allowed for access to and tight control of the mesh on each cross-section, which made it possible to construct a 3D mesh. The addition of semi-artificial nasopharynx regions to Subjects 12, 14, and 18 allowed us to proceed with numerically converged simulations.

General Flow Patterns

Individual streamline analysis can give a general sense of airflow patterns, but a full picture of the flow

features was best realized when streamline analysis was combined with velocity vector plots and computations of helicity. Rather than focusing on the path of single massless particles, these measurements provide an overall quantification of dominating flow trends. Quantification of helicity may also provide insight into differences in nasal filtering abilities. The larger helicity values found in some subjects indicated increased mixing of the inhaled air which may lead to higher particle deposition and gas uptake in these individuals.

TABLE 4. Flow allocation percentages for the Turbinate cut.

Subject	Dorsal (%)	Middle (%)	Ventral (%)
A	7	53	40
12	18	38	44
14	3	53	44
18	5	59	36

See the definition of the Turbinate cut in Fig. 3 and the definitions of the dorsal, middle, and ventral regions in Fig. 5.

Regional Flow Allocations

In the turbinate region of the nasal passages, predicted variations in the distribution of flow did not correspond directly with regional cross-sectional area whereas flow and cross-sectional area allocation corresponded fairly well among individuals in the vestibule and nasopharynx. These differences may be a result of flow being better mixed in the vestibule and nasopharynx than in the turbinate regions.

Local Reynolds numbers remain low, even in areas of the nasal passages which are often proposed to show turbulent flow. A future study might exam further the local variations in Reynolds number and investigate the implications with regard to nasal filtering abilities. The local Reynolds number does not provide addition insight into regional flow allocation patterns.

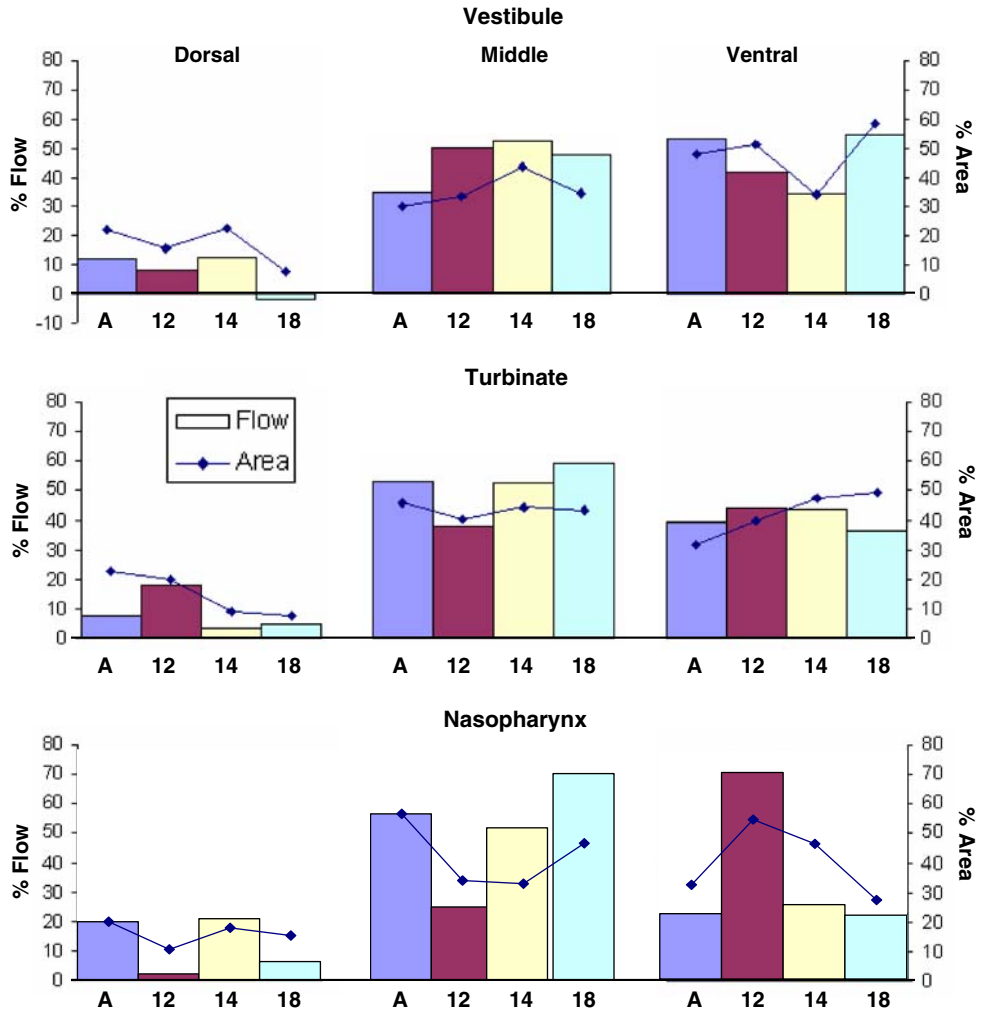

FIGURE 7. Comparison of flow allocation and cross-sectional area for the vestibule, turbinate, and nasopharynx cuts.

TABLE 5. Comparison of experimental and computational velocity values (sagittal-plane projection) for selected streamlines.

	Subject 12			Subject 14			Subject 18		
	Exp[b]	Comp[c]	% Err[d]	Exp	Comp	% Err	Exp	Comp	% Err
Vestibule[a]									
Dorsal[e]	112	130	13.8	75	67	11.9	112	105	6.7
Middle[e]	225	200	12.5	188	190	1.1	337	310	8.7
Ventral[e]	131	120	9.2	94	100	6.0	281	260	8.1
Turbinate[a]									
Dorsal	169	175	3.4	75	70	7.1	47	55	14.5
Middle	131	120	9.1	113	100	13.0	150	175	14.3
Ventral	300	310	3.2	66	62	6.4	84	85	1.2

[a]Plane of coronal cross section at which velocity measurements and computational results were obtained (see Fig. 3).
[b]Experimental measurement (cm/s).
[c]Computational result (cm/s).
[d]Percent error between experimental and computational results.
[e]Name of streamline along which velocity measurements and computational results were obtained (see Fig. 4).

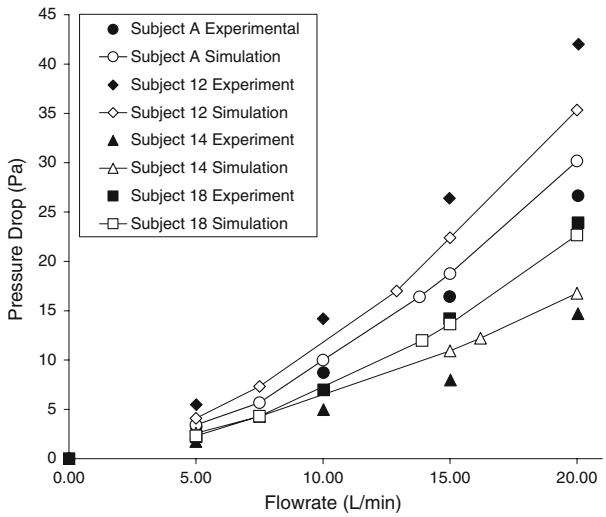

FIGURE 8. Comparison of experimental and computational results for the pressure drop between the nostril and the outlet in inspiratory flow in the four nasal models.

Experimental Confirmation

The agreement between the experimental results and the computer simulations suggests that the meshes used were sufficient to resolve a reasonable solution to the full Navier–Stokes equations and that the use of turbulence modeling is not necessary at a flow rate of 15 L/min. Although some of the Reynolds numbers for these simulations are nearing the traditional definition for the transitional flow regime (at around Re = 2000 for pipe flow), it should be emphasized that we are not simulating flow in a straight tube and therefore the traditional Reynolds number guidelines are not completely applicable in this situation.

Flow velocities were confirmed with a relatively simple water–dye method and while these confirmation experiments could not provide as complete a description of the flow field as a method like PIV, the water–dye method was much cheaper, easier, and faster to perform. Although the data obtained from the water–dye system matched well with simulation results, the sparseness of these comparisons prompted the additional confirmation step of measuring pressure drops across each model as well. The agreement of the simulation results with both streakline-specific velocity measurements and overall nasal pressure drops provided confidence in the accuracy of the computational models.

The dye used in this study remained clearly coherent for at least 1 min in still water and up to 30 s in very gently stirred water, yet dissipated completely and rapidly (in <3 s) in the presence of more vigorous stirring, even if the stirred water movement was kept laminar. For this reason, (1) flow visualization posterior to the turbinates was difficult with this dye, further necessitating the restriction of the measurements presented here to vestibular and turbinate levels, and (2) it was not possible to determine the presence or absence of turbulence in this region by dye visualization alone.

Implication of Findings

The implications of this work are that flow differences do exist among different individuals. Variation is seen in the qualitative nature of the flow, with some subjects having more swirling flow than others. Variation can also be quantified by computing flow allocation percentages. Data measurements of SAVR alone cannot account for the variation in flow allocations that is seen in the models. Furthermore, even detailed measurements of regional cross-sectional area could not predict airflow allocations. Therefore, CFD

models are needed to accurately describe flow within the nasal passages. All of the nasal models in this study were based on the nasal cavity of healthy adults and it is expected that differences within a population sample that included subjects with nasal disease would be even greater.

Due to the differences seen in flow allocation percentages, it is necessary to further extend this work to a larger population sample to include more variations in age, race, and health status. A more extensive range of subjects would lead to better statistics on the variability of the flow distribution and flow patterns. Since the turbinates are highly perfused with blood, this region is a prime location for the metabolism of inhaled material and therefore of utmost importance in characterizing an individual's susceptibility to inhaled gases and particles. In addition, as seen with Subject 12, some nasal morphologies may lead to increased flow to the olfactory region and therefore potentially increased risk to the brain via transport of material across the olfactory nerves.[7]

Current work is underway to determine the effects that flow differences have on gas uptake patterns. This work will be further extended to look at particle deposition patterns. In time, adding more nasal models to the database will allow for a more specific and quantitative measure of the intersubject variability in the dosimetry of inhaled pollutants in the nasal passages.

ACKNOWLEDGMENTS

The authors thank Ray Guilmette for his contributions, help and support, and Earl Tewksbury and Brian Wong for pressure drop data. The authors also acknowledge the excellent technical assistance of Darin Kalisak and Regina Richardson. Funding for this project was provided by the American Chemistry Council.

REFERENCES

[1]Annals of the ICRP 24; ICRP (International Commission on Radiological Protection) Publication 66. Human Respiratory Tract Model for Radiological Protection. Oxford: Pergamon Press, 1994.

[2]Batchelor, G. K. An Introduction to Fluid Dynamics. Cambridge: Cambridge University Press, 1967.

[3]Cheng, Y.-S., Y. Yamada, H.-C. Yeh, and D. L. Swift. Diffusional deposition of ultrafine aerosols in a human nasal cast. *J. Aerosol. Sci.* 19:741–751, 1988. doi:10.1016/0021−8502(88)90009-2.

[4]Chung, S. K., Y. R. Son, S. J. Shin, and S. K. Kim. Nasal airflow during respiratory cycle. *Am. J. Rhinol.* 20:379–384, 2006. doi:10.2500/ajr.2006.20.2890.

[5]Croce, C., R. Fodil, M. Durand, G. Sbirlea-Apiou, G. Caillibotte, J. F. Papon, J. R. Blondeau, A. Coste, D. Isabey, and B. Louis. In vitro experiments and numerical simulations of airflow in realistic nasal airway geometry. *Ann. Biomed. Eng.* 34:997–1007, 2006. doi:10.1007/s10439-006-9094-8.

[6]Elad, D., S. Naftali, M. Rosenfeld, and M. Wolf. Physical stresses at the air-wall interface of the human nasal cavity during breathing. *J. Appl. Physiol.* 100:1003–1010, 2006. doi:10.1152/japplphysiol.01049.2005.

[7]Erikson, K. M., D. C. Dorman, L. H. Lash, and M. Aschner. Manganese inhalation by rhesus monkeys is associated with brain regional changes in biomarkers of neurotoxicity. *Toxicol. Sci.* 97:459–466, 2007. doi:10.1093/toxsci/kfm044.

[8]FIDAP. FIDAP Theoretical Manual. Lebanon, NH: Fluent, Inc., 1991.

[9]Grigioni, M., C. Daniele, U. Morbiducci, C. Del Gaudio, G. D'Avenio, A. Balducci, and V. Barbaro. A mathematical description of blood spiral flow in vessels: application to a numerical study of flow in arterial bending. *J. Biomech.* 38:1275–1386, 2005.

[10]Guilmette, R. A., Y. S. Cheng, and W. C. Griffith. Characterizing the variability in adult human nasal airway dimensions. *Ann. Occup. Hyg.* 41(Suppl. 1):491–496, 1997.

[11]Horschler, I., M. Meinke, and W. Schroder. Numerical simulation of the flow field in a model of the nasal cavity. *Comput Fluid* 32:39–45, 2003. doi:10.1016/S0045-7930(01)00097-4.

[12]Kelly, J. T., B. Asgharian, J. S. Kimbell, and B. A. Wong. Particle deposition in human nasal airway replicas manufactured by different methods. Part I: Inertial regime particles. *Aerosol. Sci. Technol.* 38:1063–1071, 2004.

[13]Kelly, J. T., A. K. Prasad, and A. S. Wexler. Detailed flow patterns in the nasal cavity. *J. Appl. Physiol.* 89:323–337, 2000.

[14]Keyhani, K., P. W. Scherer, and M. M. Mozell. Numerical simulation of airflow in the human nasal cavity. *J. Biomech. Eng.* 117:429–441, 1995.

[15]Kim, J. K., J-H. Yoon, C. H. Kim, T. W. Nam, D. B. Shim, and H. A. Shin. Particle image velocimetry measurements for the study of nasal airflow. *Acta Oto-Laryngol.* 126:282–287, 2006.

[16]Kimbell, J. S., and R. P. Subramaniam. Use of computational fluid dynamics models for dosimetry of inhaled gases in the nasal passages. *Inhalat. Toxicol.* 13:325–334, 2001. doi:10.1080/08958370151126185.

[17]Lang, J. Clinical Anatomy of the Nose, Nasal Cavity and Paranasal Sinuses. New York: Thieme Medical, 1989.

[18]Lindemann, J., T. Keck, K. Wiesmiller, B. Sander, H.-J. Brambs, G. Rettinger, and D. Pless. A numerical simulation of intranasal air temperature during inspiration. *Laryngoscope* 114:1037–1041, 2004. doi:10.1097/00005537-200406000-00015.

[19]Liu, Y., E. A. Matida, J. Gu, and M. R. Johnson. Numerical simulation of aerosol deposition in a 3-D human nasal cavity using RANS, RANS/EIM, and LES. *J. Aerosol. Sci.* 28:683–700, 2007. doi:10.1016/j.jaerosci.2007.05.003.

[20]Longest, P. W., and S. Vinchurkar. Effects of mesh style and grid convergence on particle deposition in bifurcating airway models with comparisons to experimental data.

Med. Eng. Phys. 29:350–366, 2006. doi:10.1016/j.medengphy.2006.05.012.

[21]Martonen, T. B., Z. Zhang, G. Yue, and C. J. Musante. 3-D Particle transport within the human upper respiratory tract. *J. Aerosol. Sci.* 33:1095–1110, 2002. doi:10.1016/S0021-8502(02)00060-5.

[22]Menache, M. G., L. M. Hanna, E. A. Gross, S. R. Lou, S. J. Zinreich, D. A. Leopold, A. M. Jarabek, and F. J. Miller. Upper respiratory tract surface areas and volumes of laboratory animals and humans: considerations for dosimetry models. *J. Toxicol. Environ. Health.* 50:475–506, 1997. doi:10.1080/00984109708984003.

[23]Mlynski, G., S. Grutzenmacher, S. Plontke, B. Mlynski, and C. Lang. Correlation of nasal morphology and respiratory function. *Rhinology* 39:197–201, 2001.

[24]Park, K. I., C. Burcker, and W. Limberg. Experimental study of velocity fields in a model of human nasal cavity by DPIV. In: Laser Anemometry Advances and Applications: Proceedings of the 7th International Conference. Karlsruhe, Germany: German Association for Laser Anemometry GALA e.V., 1997, pp. 617–626.

[25]Shi, H., C. Kleinstreuer, and Z. Zhang. Laminar airflow and nanoparticle or vapor deposition in a human nasal cavity model. *J. Biomech. Eng. Trans. ASME.* 128:697–706, 2006. doi:10.1115/1.2244574.

[26]Subramaniam, R. P., R. B. Richardson, K. T. Morgan, J. S. Kimbell, and R. A. Guilmette. Computational fluid dynamics simulations of inspiratory airflow in the human nose and nasopharynx. *Inhalat. Toxicol.* 10:91–120, 1998. doi:10.1080/089583798197772.

[27]Weinhold, N., and G. Mlynski. Numerical simulation of airflow in the human nose. *Eur. Arch. Oto-rhino-laryngol.* 261:452–455, 2004. doi:10.1007/s00405-003-0675-y.

[28]Zamankhan, P., G. Ahmadi, Z. C. Wang, P. K. Hopke, Y. S. Cheng, W. C. Su, and D. Leonard. Airflow and deposition of nano-particles in a human nasal cavity. *Aerosol. Sci. Technol.* 40:463–476, 2006. doi:10.1080/02786820600660903.